Electrical Resistance of Long Conjugated Molecular Wires

Seong Ho Choi, *et al.*

Science **320**, 1482 (2008);
DOI: 10.1126/science.1156538

opens the pathway toward the imaging of larger molecules. Taken together, we can obtain a full picture of molecules. With the extension of these tools to pump-probe techniques, we will be able to simultaneously trace the temporal changes in the nuclear and electronic structure of molecules.

References and Notes

1. G. Binning, H. Rohrer, C. Gerber, E. Weibel, *Phys. Rev. Lett.* **49**, 57 (1982).
2. J. Muth-Böhm, A. Becker, F. Faisal, *Phys. Rev. Lett.* **85**, 2280 (2000).
3. X. Tong, Z. Zhao, C. Lin, *Phys. Rev. A* **66**, 033402 (2002).
4. A. Alnaser *et al.*, *Phys. Rev. A* **71**, 031403 (2005).
5. D. Pavičić, K. Lee, D. Rayner, P. B. Corkum, D. M. Villeneuve, *Phys. Rev. Lett.* **98**, 243001 (2007).
6. T. Zuo, A. Bandrauk, P. B. Corkum, *Chem. Phys. Lett.* **259**, 313 (1996).
7. H. Ihee *et al.*, *Science* **291**, 458 (2001).
8. B. J. Siwick, J. R. Dwyer, R. E. Jordan, R. J. D. Miller, *Science* **302**, 1382 (2003).
9. H. Niikura *et al.*, *Nature* **417**, 917 (2002).
10. P. B. Corkum, *Phys. Rev. Lett.* **71**, 1994 (1993).
11. J. Itatani *et al.*, *Nature* **432**, 867 (2004).
12. A. Staudte *et al.*, *Phys. Rev. Lett.* **99**, 263002 (2007).
13. A. Rudenko *et al.*, *Phys. Rev. Lett.* **99**, 263003 (2007).
14. J. Ullrich *et al.*, *Rep. Prog. Phys.* **66**, 1463 (2003).
15. H. Stapelfeldt, T. Seideman, *Rev. Mod. Phys.* **75**, 543 (2003).
16. N. B. Delone, V. P. Krainov, *J. Opt. Soc. Am. B* **8**, 1207 (1991).
17. M. Spanner, O. Smirnova, P. B. Corkum, M. Ivanov, *J. Phys. B* **37**, L243 (2004).
18. M. Ivanov, M. Spanner, O. Smirnova, *J. Mod. Opt.* **52**, 165 (2005).
19. T. Brabec, M. Ivanov, P. B. Corkum, *Phys. Rev. A* **54**, R2551 (1996).
20. D. Comtois *et al.*, *J. Phys. B* **38**, 1923 (2005).
21. J. Itatani *et al.*, *Phys. Rev. Lett.* **88**, 173903 (2002).
22. M. Lein, J. Marangos, P. Knight, *Phys. Rev. A* **66**, 051404 (2002).
23. S. Yurchenko, S. Patchkovskii, I. Litvinyuk, P. B. Corkum, G. Yudin, *Phys. Rev. Lett.* **93**, 223003 (2004).
24. D. Akoury *et al.*, *Science* **318**, 949 (2007).
25. M. Okunishi *et al.*, *Phys. Rev. Lett.* **100**, 143001 (2008).
26. C. Bordas, F. Paulig, H. Helm, D. Huestis, *Rev. Sci. Instrum.* **67**, 2257 (1996).
27. A. Eppink, D. Parker, *Rev. Sci. Instrum.* **68**, 3477 (1997).
28. I. Hartl *et al.*, *Opt. Lett.* **32**, 2870 (2007).
29. M. Lezius *et al.*, *Phys. Rev. Lett.* **86**, 51 (2001).
30. T. Kanai, S. Minemoto, H. Sakai, *Nature* **435**, 470 (2005).
31. S. Baker *et al.*, *Science* **312**, 424 (2006), published online 1 March 2006; 10.1126/science.1123904.
32. F. Légaré *et al.*, *Phys. Rev. A* **72**, 052717 (2005).
33. T. Ergler *et al.*, *Phys. Rev. Lett.* **97**, 193001 (2006).
34. A. Alnaser *et al.*, *Phys. Rev. A* **72**, 030702 (2005).

35. We gratefully acknowledge financial support from the Canadian Institute for Photonics Innovation, Natural Sciences and Engineering Research Council of Canada, Canadian Foundation for Innovation, Alexander-von-Humboldt Foundation, Deutsche Forschungsgemeinschaft, and the German Academic Exchange Service. P.B.C. acknowledges financial support from the Air Force Office of Scientific Research. M.M. thanks the German National Academic Foundation.

Supporting Online Material

www.sciencemag.org/cgi/content/full/320/5882/1478/DC1
SOM Text
Figs. S1 to S3
References

18 March 2008; accepted 16 May 2008
10.1126/science.1157980

Electrical Resistance of Long Conjugated Molecular Wires

Seong Ho Choi, BongSoo Kim, C. Daniel Frisbie*

The charge transport mechanism of a wire can be revealed by how its electrical resistance varies with length. We have measured the resistance and current-voltage characteristics of conjugated molecular wires ranging in length from 1 to 7 nanometers, connected between metal electrodes. We observe the theoretically predicted change in direct-current transport from tunneling to hopping as a function of systematically controlled wire length. We also demonstrate that site-specific disruption of conjugation in the wires greatly increases resistance in the hopping regime but has only a small effect in the tunneling regime. These nanoscale transport measurements elucidate the role of molecular length and bond architecture on molecular conductivity and open opportunities for greater understanding of electrical transport in conjugated polymer films.

Charge transport can occur through long, π-conjugated molecules (*1*–*3*), and the term "molecular wire" is often used to describe conjugated molecules in which charge transport is efficient over long distances (*4*, *5*). For example, the β-carotene molecule can transfer electrons over tens of Angstroms (*6*). In the context of molecular electronics, where the ultimate goal is the fabrication of circuitry based on the prescribed electronic function of individual molecules (*4*, *7*), it is desirable to have a quantitative definition of what constitutes a molecular wire.

A fundamental property of a wire is the scaling of its resistance (or conductance) with length. The length dependence of resistance is a direct consequence of the charge transport mechanism. In the macroscopic world, the resistance of a metallic wire increases linearly with length as a result of the diffusive nature of carrier transport in the metal. However, this particular scaling need not hold for conduction in molecules over nanometer-length scales, as has been pointed out theoretically (*8*–*10*) and observed experimentally (*2*, *3*, *11*, *12*). For short molecules (<3 nm) connected between metallic contacts, it is well-accepted that resistance scales exponentially with length according to Eq. 1.

$$R = R_0 \exp(\beta L) \quad (1)$$

where R is the junction resistance, R_0 is an effective contact resistance, L is molecular length, and β is the exponential prefactor that depends on the nature of bonding in the molecular backbone. The exponential length dependence in Eq. 1 results directly from the transport mechanism in metal/molecule/metal junctions based on short molecules, namely, direct (nonresonant) tunneling.

For longer molecules connected between metal electrodes, the scaling of resistance with length can be anticipated by comparison to fundamental studies of electron transfer in solution. Both theory and experiment on soluble donor-bridge-acceptor (D-B-A) systems (*2*, *3*, *8*, *11*, *12*) indicate that for long molecular bridges, the charge transport mechanism changes from direct tunneling to hopping, as evidenced by a change in the length dependence of the electron transfer rate constant. Specifically, for short bridges, the length dependence is exponential, corresponding to the tunneling regime, and for long bridges, the scaling is linear, as expected for hopping transport; in the experiments reported by Wasielewski and colleagues (*2*), the transition occurs when the conjugated bridge becomes longer than ~2.5 nm. The weaker length dependence associated with the hopping regime facilitates the transport of charge over greater distances, and it is this regime that might be considered most "wirelike," although tunneling through saturated peptide bonds, for example, has also been shown to provide enhanced transport over relatively large distances in redox proteins (*13*, *14*).

In the context of molecular electronics, it has been difficult to systematically examine the hopping regime in conjugated molecular wires connected to metallic contacts because of the relatively large range of molecular lengths required (spanning many nanometers) and the complexities of adsorbing long molecules to metal surfaces while controlling orientation. Electrical transport measurements on molecules up to 18 nm in length have been reported (*15*), and charge hopping in molecular junctions has been observed (*16*–*18*), but the systematic length dependence of conduction has not been a principal focus.

Here, we provide direct evidence for a change in transport mechanism from tunneling to hopping in molecular junctions based on conjugated oligophenyleneimine (OPI) wires ranging in length from 1.5 to 7.3 nm. We contacted OPI

Department of Chemistry and Department of Chemical Engineering and Materials Science, University of Minnesota, Minneapolis, MN 55455, USA.

*To whom correspondence should be addressed: frisbie@cems.umn.edu

wires grown from one electrode using controlled aryl imine addition chemistry; a metal-coated atomic force microscope (AFM) tip was used to make the second contact. We show that near 4 nm in length, the mechanism of transport in the wires changes abruptly, as evidenced by striking changes in the length, temperature, and electric field dependence of the current-voltage (*I-V*) characteristics. For longer wires, an analysis of the bias dependence established at least three different regimes of transport and provided an estimate of the single-wire conductivity. Overall, these experiments open considerable opportunities to probe the physical organic chemistry of molecular conduction, e.g., the roles of specific functional groups and bonding architectures on hopping transport in molecular wires.

OPI wires on gold substrates were prepared by a slight modification of a previously reported method (*19*). Figure 1A shows the molecular structure of OPI wire precursors (OPI-p) and OPI wires, as well as synthetic routes. The growth of OPI wires begins with OPI 1-p, prepared by immersing gold substrates into 1 mM 4-aminobenzenethiol in absolute ethanol for 24 hours. OPI-p wires were then grown by step-wise imination, with alternate addition of benzene-1,4-dicarboxaldehyde and benzene-1,4-diamine, as shown in Fig. 1A. Each OPI-p wire terminated with $–NH_2$ or –CHO groups was end-capped with benzaldehyde or aniline, respectively. The end-capping provided a consistent terminal group throughout the OPI series that facilitated reproducible electrical characterization. After each growth, both OPI-p and OPI monolayers were thoroughly rinsed with absolute ethanol and then dried in a stream of N_2.

Both OPI-p and OPI monolayers were characterized extensively by ellipsometry, x-ray photoelectron spectroscopy (XPS), reflection-absorption Fourier transform infrared spectroscopy (RAIRS), and cyclic voltammetry (CV). Key results are summarized in Table 1 as well as in the supporting online material (*20*). Monolayer thickness from ellipsometry and XPS measurements increased gradually, as expected, upon repeated imination. From the difference between estimated wire length and the measured monolayer thickness, we conclude that the OPI wires are tilted with an angle increasing from 20° to 45° with respect to the surface normal as wire length increases.

The RAIRS data, shown in Fig. 1B (left), reveal the alternate appearance and disappearance of carbonyl stretches (1710 cm^{-1}) and symmetric amine stretches (3350 cm^{-1}) in OPI-p molecules, which verified the imination mechanism and indicated near quantitative reaction of all exposed reactive end groups. The intensity of imine stretching (1620 cm^{-1}) and the benzene ring vibrational mode (1500 cm^{-1}) increased with the number of repeat units, as expected. Complete end-capping was confirmed by the disappearance of the terminal group vibrational modes in Fig. 1B (right).

Cyclic voltammograms (CV) of OPI wires are displayed in fig. S5 (*20*), and oxidation potentials and the estimated surface coverages for each OPI wire are compiled in Table 1 and table S2 (*20*). The CV sweeps of the OPI wires show nearly identical surface coverage (2.5×10^{-10} to 5.5×10^{-10} mol/cm^2) over the entire set of wires. Evidently, packing density is not greatly affected by molecular length. Collectively, the surface characterization data indicate that high-quality monolayers of OPI wires were prepared.

We investigated the transport characteristics of OPI wires using a conducting probe (CP) AFM (fig. S1), which has been used to measure conduction in a variety of molecular systems (*21*–*23*). In the semilog plot of resistance (*R*) versus molecular length (*L*) (Fig. 2A), each data point represents the average of 10 *I-V* traces. A clear transition of the length dependence of resistance is observed near 4 nm (OPI 5), indicating that the conduction mechanism is different in short (OPI 1 to 4) and long (OPI 6 to 10) OPI wires. In short wires, the linear fit in Fig. 2A indicates that the data are well described by Eq. 1 for nonresonant tunneling. The β value is found to be 3 nm^{-1}, which is within the range of β values of typical conjugated molecules (*24*, *25*).

For long OPI wires, there is a much flatter resistance versus molecular length relation (β ~ 0.9 nm^{-1}). The extremely small β suggests that the principal transport mechanism is hopping, as has been concluded in solution electron transfer studies of D-B-A systems (*2*, *11*, *26*). A plot of *R* versus *L* (Fig. 2A, inset) for long wires is linear, which is consistent with hopping and indicates that Eq. 1 does not apply for long wires. The change in transport mechanism apparent in the length-dependent measurements was verified by the temperature dependence. Figure 2B shows that resistance for OPI 4 is independent of temperature from 246 to 333 K, as expected for tunneling. However, both OPI 6 and OPI 10 display the strongly thermally activated transport that is characteristic of hopping. The activation energies determined from the slopes of the data are identical at 0.28 eV (6.5 kcal/mol) for both OPI 6 and

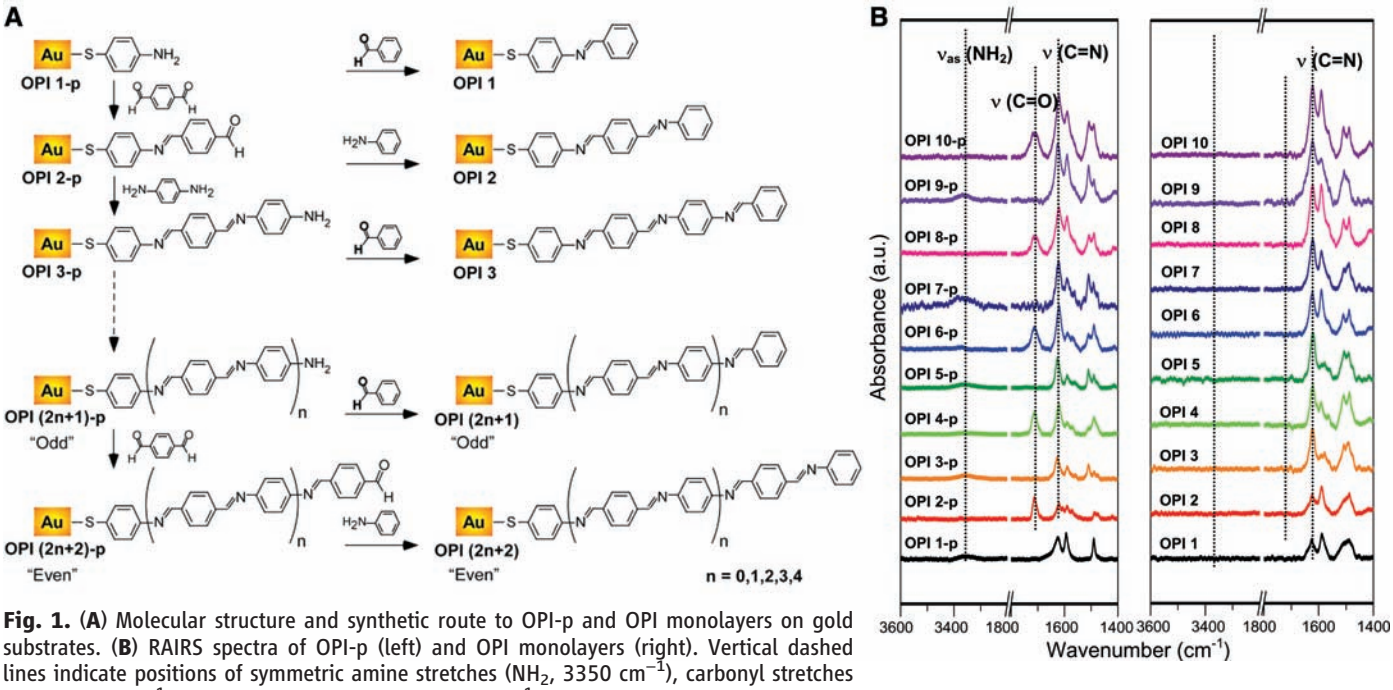

Fig. 1. (**A**) Molecular structure and synthetic route to OPI-p and OPI monolayers on gold substrates. (**B**) RAIRS spectra of OPI-p (left) and OPI monolayers (right). Vertical dashed lines indicate positions of symmetric amine stretches (NH_2, 3350 cm^{-1}), carbonyl stretches (C=O, 1710 cm^{-1}), and imine stretches (C=N, 1620 cm^{-1}). Peaks for NH_2 and C=O appear in the uncapped OPI-p wires with odd and even numbers of repeat units, respectively.

OPI 10. Contact effects are not responsible for the activated transport, because straightforward calculation shows that the injection efficiency is >99% (*27*). Collectively, the data in Fig. 2 indicate that the conduction mechanism transitions from tunneling to hopping near 4 nm.

Questions remain concerning the nature of the hopping sites in the long wires and the origin of the 0.28 eV activation energy. Electronic delocalization is limited in aromatic oligoimines because of the nonzero dihedral angle between the benzene ring and the imine bonds (*28*), that is, the wire molecules are not flat and the π-conjugation is broken. We have confirmed by ultraviolet-visible absorption spectroscopy that the conjugation does not extend over the entire wire (*20*). The optical gap (E_g) reduces with molecular length up to OPI 3 and then remains constant at 2.6 eV for longer OPI wires (Table 1). This result indicates that the π-conjugation extends over three repeating units by means of the imine linkage and that longer wires contain weakly linked conjugated subunits.

We propose that the short, three-repeat conjugated subunits are the charge-hopping sites in the wires and that the hopping activation energy corresponds to the barrier for rotation of the aromatic rings, which transiently couples the conjugated subunits. Charges are driven down the wires as the conjugation fluctuations permit. Torsional vibrations of the rings in analogous aromatic oligoimines are accompanied by coupled alterations of the C=N bond length, and this concerted motion is likely responsible for transiently coupling the conjugated subunits (*29*). The energy associated with these collective motions is indeed ~0.3 eV (*29*, *30*), which is comparable to the observed hopping barrier. From the slope of R versus L in Fig. 2 and the estimated number of wires in the junction (~100), we calculated a single-wire conductivity of 1×10^{-6} S/cm. This low value must reflect the low density of carriers in the wires and the significant hopping activation energy (*31*–*33*).

To examine the sensitivity of conduction to the wire architecture, we designed conjugation-broken OPI wires (CB-OPIs) in which an aliphatic cyclohexyl group was inserted into the molecular backbone. To incorporate the cyclohexyl moiety, we performed the imination with 1,4-diaminocyclohexane at elevated temperature (40°C) in pure ethanol for 24 hours. The structure of CB-OPI wires and their low voltage resistances are shown in Fig. 3. For CB-OPI 3 and CB-OPI 4, the resistance is increased compared with OPI 3 and OPI 4, as expected, because the aliphatic cyclohexyl links raise the average tunneling barrier. However, for the longer CB-OPI 8 and CB-OPI 10 molecules, the resistance change from the corresponding OPI 8 and OPI 10 wires is considerably greater, nearly two orders of magnitude.

Evidently, conduction in the long wires is much more sensitive to the presence of the cyclohexyl group than in the short wires, which also supports a difference in the charge transport mechanism. For hopping transport in the long wires, a large change in resistance is expected upon interrupting the conjugation. Ratner and colleagues (*34*, *35*) have calculated the site-to-site hopping probabilities for molecular wires and, indeed, a disruption in conjugation has a dramatic impact on electron transfer rates. However, tunneling is relatively insensitive to small perturbations in the conjugation of molecular bridges, because the tunneling rate reflects the average potential barrier of the bridge, not the barrier of the discrete cyclohexyl group alone. Thus, the conjugation blocking experiments confirm that conduction depends on the bond architecture, and they also support the conclusion that tunneling occurs in the short wires and hopping transport prevails in the long wires.

We have also carefully examined the voltage and electric field dependence of the *I*-*V* characteristics (Fig. 4). The semilog plot of I versus V for OPI wires in Fig. 4A demonstrates that current decreases as wire length increases, in keeping with the resistance results shown in Fig. 2. For the short wires (OPI 1 to 4), increasing molecular length yields large decreases in the current at all potentials. However, for the long wires (OPI 6 to 10), the log *I*-*V* curves show smaller decreases in current with increasing length. A plot of log I versus electric field E (Fig. 4A, inset) reveals that the traces for the long wires collapse nearly on top of one another. This result indicates that for

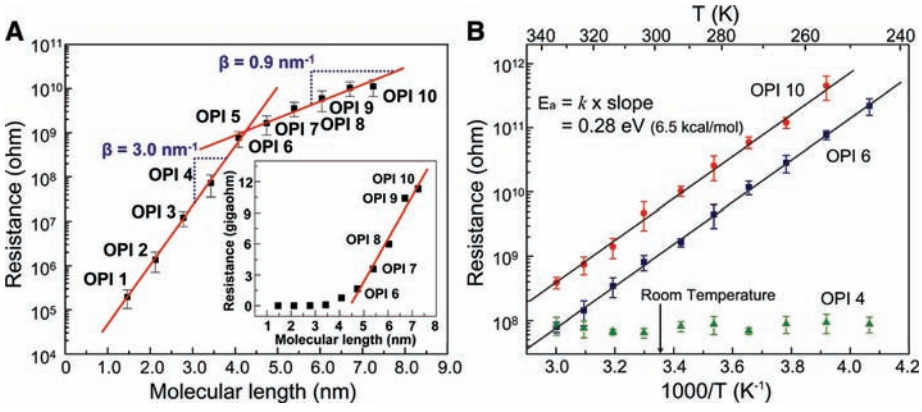

Fig. 2. Measurements of molecular wire resistance with CP-AFM. A gold-coated tip was brought into contact with an OPI monolayer on a gold substrate. The *I*-*V* traces were obtained over ±1.5 V for OPI 3 to 10 and ±1.0 V for OPI 1 and 2 at a load of 2 nN on the tip contact. (**A**) Semilog plot of R versus L for the gold/wire/gold junctions. Each data point is the average differential resistance obtained from 10 *I*-*V* traces in the range −0.3 to +0.3 V. Error bars, 1 SD. Straight lines are linear fits to the data according to Eq. 1. (Inset) A linear plot of R versus L, demonstrating linear scaling of resistance with length for the long OPI wires. (**B**) Arrhenius plot for OPI 4, OPI 6, and OPI 10. Each data point is the average differential resistance obtained at six different locations on samples in the range −0.2 to +0.2 V. Error bars, 1 SD. Straight lines are linear fits to the data.

Table 1. Selected experimental and calculated data for OPI wires. Molecular length was estimated with the Cambridge Scientific Chem3D software. Molecular length is the terminal H to S distance plus the Au-S bond length. It was assumed that Au-S bond length is 2.36 Å (*41*). Film thickness is from ellipsometry and XPS; the XPS data are underestimated because the intensity of photoelectrons from N atoms is not considered in the calculation of film thickness. The oxidation potentials were determined from the lower edge of the oxidation peak of OPI wires referenced to ferrocenium/ferrocene (Fc^+/Fc).

Monolayer	Estimated molecular length (nm)	Film thickness (by ellipsometry/XPS) (nm)	E_g (eV)	Oxidation potential (V)	n in I, I′ $I \propto V^n$	n in II′ $I \propto V^n$	V_{trans} (V) [E_{trans} (MV/cm)]	$V_{II'}$ (V) [$E_{II'}$ (MV/cm)]	ϕ_{FE} (eV)
OPI 2	2.1	1.8 / 1.6	3.1	0.22	1.1	–	0.85 [4.0]	–	–
OPI 3	2.8	2.5 / 1.9	2.6	0.14	1.1	–	0.75 [2.7]	–	–
OPI 4	3.4	3.0 / 2.1	2.6	0.06	1.3	–	0.75 [2.2]	–	–
OPI 6	4.7	4.1 / 2.7	2.6	0.05	1.2	2.6	1.00 [2.1]	0.5 [1.0]	0.3–0.5
OPI 10	7.3	5.3 / 4.0	2.6	0.00	0.9	2.6	0.95 [1.3]	0.40 [0.6]	0.3–0.5

the long wires, transport is field driven, as expected for a hopping mechanism in which the electric field pushes the carriers along the molecules. However, for the short wires, the *I-E* curves do not collapse on top of one another because tunneling is a voltage-driven process.

A log-log plot of the *I-V* characteristics facilitates more detailed analysis. Figure 4B displays log *I*–log *V* characteristics for OPI 4 and OPI 10, representative of the short and long wires. For OPI 4, there are two different transport regimes, labeled I and II; the transition occurs at 0.75 V. For OPI 10, the dependence is more complex, with three identifiable transport regimes (I′, II′, and III′) and transitions at 0.40 V and 0.95 V.

The data for OPI 4 in Fig. 4B demonstrate that, in regime I, the current scales linearly with voltage. Linear *I-V* behavior is expected for tunneling in the low-bias regime. To a first approximation, the metal/wire/metal junction can be modeled as a simple trapezoidal tunneling barrier. In this case, the tunneling current at low bias is given by Eq. 2.

$$I \propto V \exp\left(-\frac{2d\sqrt{2m_e\phi}}{\hbar}\right) \quad (2)$$

where d is the barrier width (wire length), m_e is the electron effective mass, and ϕ is the effective barrier height. At higher bias, the electric field changes the shape of the tunneling barrier from trapezoidal to triangular (*36*). In this case, the *I-V* behavior can be described by the Fowler-Nordheim relation:

$$\ln\left(\frac{I}{V^2}\right) \propto \frac{-4d\sqrt{2m_e\phi^3}}{3\hbar q}\left(\frac{1}{V}\right) \quad (3)$$

where q is the elementary charge.

The Fowler-Nordheim plot in Fig. 4C reveals a striking change in conduction behavior. For low voltages (Regime I), the current scales logarithmically with $1/V$, as expected from Eq. 2, indicative of direct tunneling. Above the transition voltage V_{trans} = 0.75 V (Regime II), the current scales linearly with $1/V$, with a negative slope characteristic of field emission (Eq. 3). The transition point, V_{trans}, is an estimate of the low voltage barrier height and corresponds to the voltage where the slope of the OPI 4 data changes in Fig. 4B. The V_{trans} values for the other short OPI wires are listed in table S1. The decrease of V_{trans} with length in short wires indicates that the estimated barrier height decreases as expected from the trend in oxidation potentials of OPI wires determined by cyclic voltammetry (Table 1) (*20*). Collectively, the data in Figs. 2 to 4 allow us to conclude that the transport mechanism in the short wires at low bias is direct (nonresonant) tunneling and transitions to field emission at higher bias.

We have carried out a similar analysis of the *I-V* behavior for long wires, OPI 6 to 10. The Fowler-Nordheim plot for OPI 10 in Fig. 4D reveals three distinct regimes corresponding with regimes I′, II′, and III′ in Fig. 4B. In the low-bias regime I′, the current scales linearly with voltage, which is consistent with ohmic hopping conduction. Linear scaling with V was taken as support for nonresonant tunneling in short wires in the discussion above (Eq. 2), but it is already clear that the low-bias mechanisms are different for the long and short wires, and direct tunneling is not consistent with the dependences of resistance on length or temperature evident in Fig. 2B. Ohmic (field-driven) conduction is also linear in V and requires that carriers be present in the wires. We propose that carriers are introduced in the long wires from the gold contacts and that these carriers result in ohmic hopping conduction at low biases up to $V_{II'}$, the transition voltage from regime I′ to II′. The presence of carriers (most likely positively charged holes) in the wires

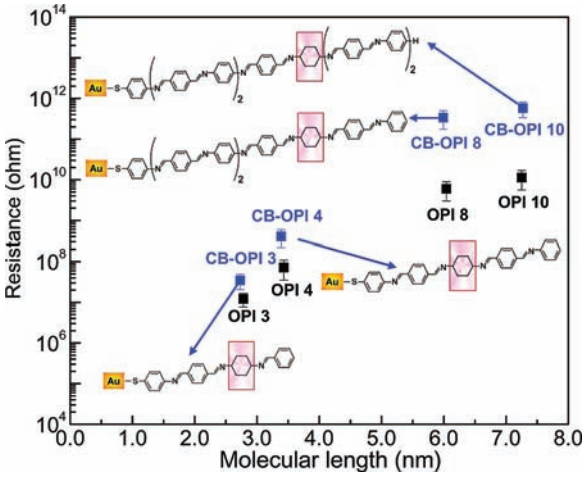

Fig. 3. Semilog plot of *R* versus *L* for gold/OPI/gold junctions and CB gold/CB-OPI/gold junctions. Each data point is the average differential resistance from 10 *I-V* traces in the interval −0.3 V to 0.3 V. Error bars, 1 SD. The blue squares are the resistances of CB-OPI wires. Pink boxes indicate the position where conjugation is broken.

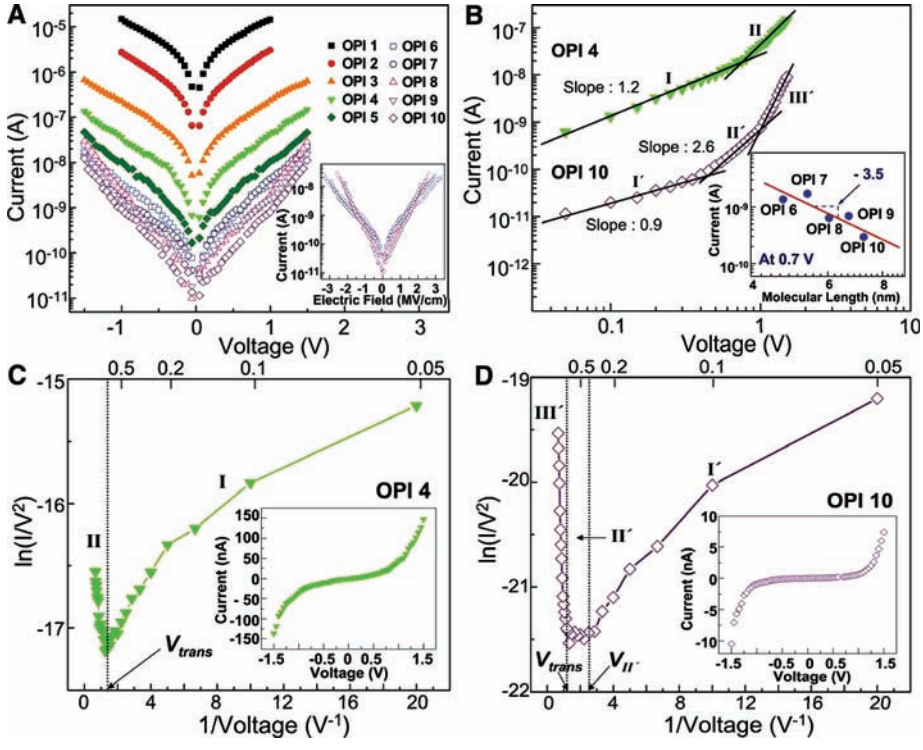

Fig. 4. (**A**) Semilog plot of the average current of 10 *I-V* traces for gold/wire/gold junctions. The inset is a semilog plot of *I* versus *E* for long OPI wires. (**B**) Log-log plot of the average of 10 *I-V* traces for the gold/OPI 4/gold and gold/OPI 10/gold junctions. Fits are shown in the different transport regimes. (Inset) A log-log plot of *I* versus *L* obtained at 0.7 V for all long OPI wires, displaying the linear fit with a slope of −3.5 (0.7 V is the bias at which all long OPI wires are within regime II′). (**C**) Fowler-Nordheim plot for the OPI 4 data in (B). Two distinct regimes (I and II) are clearly observable, with an inflection point at V_{trans}, indicating the switch from tunneling to field emission. The inset displays the sigmoidal current-voltage curve on a linear scale. (**D**) Fowler-Nordheim plot for the OPI 10 data in (B). Three distinct regimes (I′, II′, and III′) are evident. The inset shows the sigmoidal current-voltage curve.

means that the energy barrier to charge injection from the gold contacts must be smaller than the 0.7 eV E_F-E_{HOMO} offset measured by ultraviolet photoelectron spectroscopy (UPS) (*20*). Indeed, the offset will be reduced considerably by both the image potential associated with the metal contacts and the polaron shift (*16*), both of which are not accounted for in UPS measurements (*37*).

The negative slope in the high-voltage regime III′ of Fig. 4D suggests that field emission may also occur in OPI 10 (similar results were obtained for OPI 6 to 9). From the slope in regime III′, we calculated the emission barrier height (ϕ_{FE}) to be in the range of 0.3 to 0.5 eV, assuming carrier effective mass ratios in the range 0.1 to 1.0, which are typical for molecular junctions (*24*). We also considered other possible transport mechanisms in the metal/wire/metal junction, such as Schottky emission at the contact, Poole-Frenkel emission in the wires, and space-charge-limited transport in the presence of traps (*38*, *39*). However, we did not obtain reasonable values for extracted physical parameters with these other mechanisms (*20*). The estimated emission barrier heights for the other long OPI wires are also listed in Table 1 and table S1. Regime II′ is a transitional regime between ohmic conduction and field emission for OPI 10, and it may correspond to space-charge-limited conduction (SCLC), based on the slope of 2.6 in the log *I* versus log *V* plot (Fig. 4B) and the slope of –3.5 in the log *I* versus log *L* plot at 0.7 V (inset in Fig. 4B) (*39*, *40*). Further work is necessary to conclusively establish the transport mechanism in this regime.

References and Notes

1. A. Nitzan, M. A. Ratner, *Science* **300**, 1384 (2003).
2. W. B. Davis, W. A. Svec, M. A. Ratner, M. R. Wasielewski, *Nature* **396**, 60 (1998).
3. B. Giese, J. Amaudrut, A. K. Kohler, M. Spormann, S. Wessely, *Nature* **412**, 318 (2001).
4. R. L. Carroll, C. B. Gorman, *Angew. Chem. Int. Ed.* **41**, 4378 (2002).
5. H. D. Sikes *et al*., *Science* **291**, 1519 (2001).
6. J. He *et al*., *J. Am. Chem. Soc.* **127**, 1384 (2005).
7. K. S. Kwok, J. C. Ellenbogen, *Mater. Today* **5**, 28 (2002).
8. D. Segal, A. Nitzan, W. B. Davis, M. R. Wasielewski, M. A. Ratner, *J. Phys. Chem. B* **104**, 3817 (2000).
9. D. Segal, A. Nitzan, M. Ratner, W. B. Davis, *J. Phys. Chem. B* **104**, 2790 (2000).
10. Y. A. Berlin, A. L. Burin, M. A. Ratner, *Chem. Phys.* **275**, 61 (2002).
11. B. Giese, *Acc. Chem. Res.* **33**, 631 (2000).
12. E. M. Conwell, *Proc. Natl. Acad. Sci. U.S.A.* **102**, 8795 (2005).
13. D. N. Beratan, J. N. Onuchic, J. R. Winkler, H. B. Gray, *Science* **258**, 1740 (1992).
14. H. B. Gray, J. R. Winkler, *Proc. Natl. Acad. Sci. U.S.A.* **102**, 3534 (2005).
15. W. P. Hu *et al*., *Phys. Rev. Lett.* **96**, 027801 (2006).
16. S. Kubatkin *et al*., *Nature* **425**, 698 (2003).
17. Y. Selzer, M. A. Cabassi, T. S. Mayer, D. L. Allara, *J. Am. Chem. Soc.* **126**, 4052 (2004).
18. Y. Selzer *et al*., *Nano Lett.* **5**, 61 (2005).
19. J. J. W. M. Rosink *et al*., *Langmuir* **16**, 4547 (2000).
20. Materials and methods are available as supporting material on *Science* Online.
21. D. J. Wold, C. D. Frisbie, *J. Am. Chem. Soc.* **123**, 5549 (2001).
22. V. B. Engelkes, J. M. Beebe, C. D. Frisbie, *J. Am. Chem. Soc.* **126**, 14287 (2004).
23. X. D. Cui *et al*., *Science* **294**, 571 (2001).
24. A. Salomon *et al*., *Adv. Mater.* **15**, 1881 (2003).
25. M. D. Newton, *Chem. Rev.* **91**, 767 (1991).
26. F. C. Grozema, Y. A. Berlin, L. D. A. Siebbeles, *J. Am. Chem. Soc.* **122**, 10903 (2000).
27. Y. L. Shen, A. R. Hosseini, M. H. Wong, G. G. Malliaras, *Chem. Phys. Chem.* **5**, 16 (2004).
28. R. Akaba, K. Tokumaru, T. Kobayashi, *Bull. Chem. Soc. Jpn.* **53**, 1993 (1980).
29. J. Harada, M. Harakawa, K. Ogawa, *Acta Crystallogr. B* **60**, 578 (2004).
30. T. Tsuji, H. Takeuchi, T. Egawa, S. Konaka, *J. Am. Chem. Soc.* **123**, 6381 (2001).
31. F. C. Grozema *et al*., *Adv. Mater.* **14**, 228 (2002).
32. F. C. Grozema, P. T. van Duijnen, Y. A. Berlin, M. A. Ratner, L. D. A. Siebbeles, *J. Phys. Chem. B* **106**, 7791 (2002).
33. P. Prins *et al*., *Phys. Rev. Lett.* **96**, 146601 (2006).
34. Y. A. Berlin, G. R. Hutchison, P. Rempala, M. A. Ratner, J. Michl, *J. Phys. Chem. A* **107**, 3970 (2003).
35. Y. A. Berlin, M. A. Ratner, *Radiat. Phys. Chem.* **74**, 124 (2005).
36. J. M. Beebe, B.-S. Kim, J. W. Gadzuk, C. D. Frisbie, J. G. Kushmerick, *Phys. Rev. Lett.* **97**, 026801 (2006).
37. X.-Y. Zhu, *Surf. Sci. Rep.* **56**, 1 (2004).
38. S. M. Sze, *Physics of Semiconductor Devices* (Wiley, New York, 1981).
39. M. A. Lampert, *Phys. Rev.* **103**, 1648 (1956).
40. A. Rose, *Phys. Rev.* **97**, 1538 (1955).
41. J. M. Tour *et al*., *J. Am. Chem. Soc.* **117**, 9529 (1995).

42. The authors thank G. Haugstad for support in the temperature-dependent measurements and X.-Y. Zhu for help with photoelectron spectroscopy. This work was supported primarily by the National Science Foundation under CHE-0616427. Partial support for facilities was provided by the NSF Materials Research Science and Engineering Centers program under DMR-0212302. Parts of this work were carried out in the Institute of Technology Characterization Facility, University of Minnesota, which receives partial support from NSF through the National Nanotechnology Infrastructure Network program.

Supporting Online Material

www.sciencemag.org/cgi/content/full/320/5882/1482/DC1
Materials and Methods
SOM Text
Figs. S1 to S8
Tables S1 and S2
References

15 February 2008; accepted 9 May 2008
10.1126/science.1156538

The Impact of Stratospheric Ozone Recovery on the Southern Hemisphere Westerly Jet

S.-W. Son,[1]* L. M. Polvani,[1,2] D. W. Waugh,[3] H. Akiyoshi,[4] R. Garcia,[5] D. Kinnison,[5] S. Pawson,[6] E. Rozanov,[7,8] T. G. Shepherd,[9] K. Shibata[10]

In the past several decades, the tropospheric westerly winds in the Southern Hemisphere have been observed to accelerate on the poleward side of the surface wind maximum. This has been attributed to the combined anthropogenic effects of increasing greenhouse gases and decreasing stratospheric ozone and is predicted to continue by the Intergovernmental Panel on Climate Change/Fourth Assessment Report (IPCC/AR4) models. In this paper, the predictions of the Chemistry-Climate Model Validation (CCMVal) models are examined: Unlike the AR4 models, the CCMVal models have a fully interactive stratospheric chemistry. Owing to the expected disappearance of the ozone hole in the first half of the 21st century, the CCMVal models predict that the tropospheric westerlies in Southern Hemisphere summer will be decelerated, on the poleward side, in contrast with the prediction of most IPCC/AR4 models.

Recent observations (*1*–*4*) indicate that the westerly jet in the Southern Hemisphere (SH) troposphere is accelerating on the poleward side; this is usually described as a positive trend of the Southern annular mode index (*1*). This acceleration has important consequences for SH climate: It directly affects the surface temperatures (*2*), the extent of sea ice (*2*), the variability of storm tracks (*5*), the location of arid regions (*6*), the strength of the wind-driven oceanic circulation (*7*), and the exchange of CO_2 and heat between atmosphere and ocean (*7*, *8*). Understanding and predicting changes in the SH westerlies are therefore of the utmost importance.

Climate models have shown that the recent wind changes likely result from an increase in greenhouse gases and the depletion of stratospheric ozone (*9*–*11*), but the relative contribution of these two effects remains an open question, especially for the 21st century when stratospheric ozone is expected to recover as a result of the implementation of the Montreal Protocol (*12*). The multimodel mean of the IPCC/AR4 atmosphere-ocean–coupled model integrations indicates that the acceleration of the SH westerlies on the

[1]Department of Applied Physics & Applied Mathematics, Columbia University, New York, NY 10027, USA. [2]Department of Earth and Environmental Sciences, Columbia University, New York, NY 10027, USA. [3]Department of Earth and Planetary Sciences, Johns Hopkins University, Baltimore, MD 21218, USA. [4]National Institute for Environmental Studies, Tsukuba, Japan. [5]National Center for Atmospheric Research (NCAR), Boulder, CO 80325, USA. [6]NASA/Goddard Space Flight Center, Greenbelt, MD 20771, USA. [7]Institute for Atmospheric and Climate Sciences/Eidgenössische Technische Hochschule (ETH), Zurich, Switzerland. [8]Physical Meteorological Observatory, World Radiation Center, Davos, Switzerland. [9]Department of Physics, University of Toronto, Toronto, Canada. [10]Meteorological Research Institute, Tsukuba, Japan.

*To whom correspondence should be addressed. E-mail: sws2112@columbia.edu